

H. Uchida^{8,*}, K. Abe^{1,3}, K. Hieda¹, K. Hiraide^{1,3}, S. Hirano¹, K. Ichimura¹,
Y. Kishimoto^{1,3}, K. Kobayashi^{1,3}, S. Moriyama^{1,3}, K. Nakagawa¹, M. Nakahata^{1,3},
H. Ogawa^{1,3}, N. Oka¹, H. Sekiya^{1,3}, A. Shinozaki¹, Y. Suzuki^{1,3}, A. Takeda^{1,3},
O. Takachio¹, D. Umemoto¹, M. Yamashita^{1,3}, B. S. Yang¹, S. Tasaka², J. Liu³,
K. Martens³, K. Hosokawa⁵, K. Miuchi⁵, A. Murata⁵, Y. Onishi⁵, Y. Otsuka⁵,
Y. Takeuchi^{5,3}, Y. H. Kim⁶, K. B. Lee⁶, M. K. Lee⁶, J. S. Lee⁶, Y. Fukuda⁷,
Y. Itow^{8,4}, K. Masuda⁸, Y. Nishitani⁸, H. Takiya⁸, N. Y. Kim⁹, Y. D. Kim⁹,
F. Kusaba¹⁰, K. Nishijima¹⁰, K. Fujii¹¹, I. Murayama¹¹, S. Nakamura¹¹

¹*Kamioka Observatory, Institute for Cosmic Ray Research, the University of Tokyo,
Higashi-Mozumi, Kamioka, Gifu, 506-1205, Japan*

²*Information and multimedia center, Gifu University, Gifu 501-1193, Japan*

³*Kavli Institute for the Physics and Mathematics of the Universe (WPI), the University of Tokyo,
Kashiwa, Chiba, 277-8582, Japan*

⁴*Kobayashi-Maskawa Institute for the Origin of Particles and the Universe, Nagoya University,
Furo-cho, Chikusa-ku, Nagoya, Aichi, 464-8602, Japan*

⁵*Department of Physics, Kobe University, Kobe, Hyogo 657-8501, Japan*

⁶*Korea Research Institute of Standards and Science, Daejeon 305-340, South Korea*

⁷*Department of Physics, Miyagi University of Education, Sendai, Miyagi 980-0845, Japan*

⁸*Solar-Terrestrial Environment Laboratory, Nagoya University, Nagoya, Aichi 464-8601, Japan*

⁹*Department of Physics, Sejong University, Seoul 143-747, South Korea*

¹⁰*Department of Physics, Tokai University, Hiratsuka, Kanagawa 259-1292, Japan*

¹¹*Department of Physics, Faculty of Engineering, Yokohama National University, Yokohama,
Kanagawa 240-8501, Japan*

*E-mail: xmass.publications@km.icrr.u-tokyo.ac.jp

.....
A search for inelastic scattering of Weakly Interacting Massive Particles (WIMPs) on
the isotope ¹²⁹Xe was done in data taken with the single phase liquid xenon detector
XMASS at the Kamioka Observatory. Using a restricted volume containing 41 kg of LXe
at the very center of our detector we observed no significant excess in 165.9 days of data
and derived for e.g. a 50 GeV WIMP an upper limit for its inelastic cross section on
¹²⁹Xe nuclei of 3.2 pb at the 90% confidence level.
.....

Subject Index C43, E64, F41

1. Introduction

There is ample observational evidence for the existence of dark matter in the Universe. All evidence is gravitational though: Observing the distribution and motion of normal matter in galaxies and clusters we derive its presence. No evidence exists for any interaction other than the gravitational one that dark matter might have with normal matter. Theory provides strong motivation to postulate WIMP dark matter. If WIMPs do indeed make up the bulk of the dark matter in the universe and its weak coupling to normal matter is strong enough, elastic scattering of nuclei should provide the experimental signature for such an interaction. Unfortunately the resulting recoil energy is very low (~ 10 keV), and the spectrum of the

recoiling nuclei is falling off exponentially, making it difficult to distinguish from backgrounds near the threshold.

Internationally significant experimental effort is expended to probe for such nuclear recoils through elastic scattering [1–9]. Inelastic scattering that excites a nucleus to suitable low lying nuclear excited states provides another avenue to probe for WIMP dark matter. Its advantage is that nuclear excited states and their de-excitation mechanisms are typically well measured, and thus the expected energy deposit in the detector is known, resulting in the readily identifiable signature of a line in the energy spectrum. Using ^{127}I there is an experimental search for this inelastic scattering with the excitation level of 57.6 keV [10, 11]. In xenon the isotope ^{129}Xe has a low lying excited state at 39.58 keV; lower than that for ^{127}I , yet significantly above both the XMASS data acquisition and analysis thresholds. The de-excitation of this M1 state in ^{129}Xe proceeds through gamma ray emission or an internal conversion electron with subsequent X-ray emission. With its high nuclear charge Xe itself is a good absorber for such gamma rays, providing liquid xenon (LXe) detectors with an intrinsically high detection efficiency for the prospective signal, which is safely above the detector threshold.

So far the DAMA group searched for this signal in a 2500 kg·day exposure of 6.5 kg of LXe. They used 99.5% enriched ^{129}Xe and constrained the inelastic cross section for 50 GeV WIMPs to be less than 3 pb at 90% confidence level (C.L.) [12, 13].

In this paper results from our own search for this signal in XMASS data is reported. Though the LXe in XMASS contains ^{129}Xe only at the level of its natural abundance, our detector’s significantly lower background and excellent light yield allowed us to be more sensitive to this inelastic scattering signal.

2. The XMASS detector

The XMASS experiment is located underground in the Kamioka Observatory at a depth of 2700 m.w.e., aiming to detect dark matter [14]. XMASS is a single phase liquid xenon scintillation detector containing 1050 kg of Xe in its OFHC copper vessel. Xenon scintillation light is detected by 642 inward-pointing Hamamatsu R10789 series photomultiplier tubes (PMTs) arranged on an 80 cm diameter pentakis-dodecahedron support structure within the LXe containment vessel to give a total photocathode coverage of 62.4 % of the detector’s inner surface. This surface encloses an active target region containing 835 kg of liquid xenon. To shield the scintillator volume from external gamma rays and neutrons, and to veto muon-induced backgrounds, this active target of outer detector is located at the center of a $\phi 10\text{ m} \times 11\text{ m}$ cylindrical tank filled with pure water. This volume is viewed by 72 Hamamatsu R3600 20-inch PMTs to provide the active muon veto as well as being a passive shield against external backgrounds. This is the first water Cherenkov shield used in a dark matter experiment.

To calibrate energy and position reconstruction a portal exists above the center of the detector. Through it radioactive calibration sources can be inserted and positioned along the central vertical axis of the inner detector. Measuring with the ^{57}Co source from the center

of the detector volume the photoelectron yield^{*1} is determined to be 13.9 photoelectrons (p.e.)/keV. A more detailed description of the XMASS detector is presented in [15].

PMT signals are passed through preamplifiers with a voltage gain factor of 11 before being processed by Analog-Timing-Modules (ATMs) [18]. These modules combine the functions of typical ADC and TDC modules, recording both the integrated charge and the arrival time of each PMT signal. For each PMT channel the discriminator threshold is set to -5 mV, which corresponds to 0.2 p.e.. When a PMT signal is above threshold a “hit” is registered on the module. A global trigger is generated if the number of hit PMTs within a 200 ns window is more than nine.

A complete XMASS detector Monte Carlo (MC) simulation package based on Geant4 [19, 20] including the readout electronics has been developed [15] and used for this analysis. The simulation has been tuned using calibration data and the optical properties of the liquid xenon have also been extracted from calibration data. The energy dependence of the light yield as well as the energy resolution were also tuned on calibration data, as were the decay constant of gamma induced scintillation light and the transit timing spread (TTS) of the PMTs. We choose these constants so that we can reproduce the observed distribution of PMT hit timing in our simulation. The effective decay constant τ_γ thus determined is 27.3 ns for a 39.58 keV gamma ray and the TTS is 2.33 ns (rms).

3. Expected Signal and Detector Simulation

WIMP on ^{129}Xe inelastic scattering produces a 39.58 keV γ -ray from de-excitation and a few keV energy deposition due to nuclear recoil. Energy spectra for the nuclear recoil part are obtained as described in Ref. [12, 13]. The differential rate for inelastic scattering of WIMPs is calculated from

$$\frac{dR}{dE_{det}} = \frac{dE_{nr}}{d(\mathcal{L}_{eff} E_{nr})} \frac{dR}{dE_{nr}} = \frac{dE_{nr}}{d(\mathcal{L}_{eff} E_{nr})} \frac{\rho_W N_T \sigma_I^{as} M_N c^2}{2M_W \mu^2} F^2(E_{nr}) \int_{v_{min}(E_{nr})}^{v_{max}} \frac{1}{v} \frac{dn}{dv} dv, \quad (1)$$

where R is event rate in a unit mass of the target, E_{det} is the detected energy in electron equivalent, E_{nr} is the recoil energy, $\mathcal{L}_{eff} = \mathcal{L}_{eff}(E_{nr})$ is a factor that converts nuclear recoil energy E_{nr} to electron equivalent energy E_{det} relative to that of 122 keV gamma at zero electric field [16, 21], ρ_W is the local mass density of dark matter ($0.3 \text{ GeV}/\text{cm}^3$) [22], N_T is the number of target nuclei, σ_I^{as} is the asymptotic cross section for inelastic scattering, M_N is the mass of the target nucleus, M_W is the WIMP mass, μ is the reduced mass of the WIMP mass and the target nucleus mass, $F^2(E_{nr})$ is the nuclear form factor of ^{129}Xe , v_{max} is the maximum velocity of the WIMPs in the Earth’s vicinity (approximated by the local escape velocity for the galaxy, 650 km/s), $v_{min}(E_{nr})$ is the minimum velocity to cause the excitation of the nuclei, v is the velocity of the WIMP, and dn/dv is the velocity distribution of WIMPs. The velocity distribution, dn/dv , is assumed to be a quasi-Maxwellian with a most probable thermal speed of the WIMPs $v_0=220$ km/s [23] and the average velocity of the Earth in the galactic frame $v_e=232$ km/s [24]. Following Ref. [12, 13], the minimum velocity

^{*1} This photoelectron yield is smaller than the value reported in Ref. [15–17] since we changed a correction on the charge observed in our electronics. This correction is within the uncertainty reported earlier [15].

needed to excite ^{129}Xe is evaluated as:

$$v_{min} = v_{min}^0 + \frac{v_{thr}^2}{4v_{min}^0}, \quad (2)$$

with:

$$v_{min}^0 = \sqrt{\frac{M_N E_{nr}}{2\mu^2}} \quad (3)$$

$$E_{det} = E^* + \mathcal{L}_{\text{eff}} E_{nr} \quad (4)$$

$$v_{thr}^2 = 2\Delta E c^2 / \mu, \quad (5)$$

where ΔE is the energy of the first excited state of ^{129}Xe (39.58 keV) and $E^* \sim \Delta E$ is the sum of all the energy deposited in the de-excitation process.

The total event rate in the case of a point-like target thus becomes:

$$R_{I,\text{point-like}} = \int_{v_{thr}}^{v_{max}} \frac{\rho_W v}{M_W} N_T \sigma_I(v) \frac{dn}{dv} dv = \frac{\rho_W \langle v \rangle}{M_W} f N_T \sigma_I^{as} \quad (6)$$

$$f = \frac{1}{\langle v \rangle} \int_{v_{thr}}^{v_{max}} (v^2 - v_{thr}^2)^{1/2} \frac{dn}{dv} dv, \quad (7)$$

where $\sigma_I(v)$ is the excitation cross section for a point-like target, which is expressed as the following function of the WIMP velocity v :

$$\sigma_I(v) = \frac{\mu^2}{\pi M_N} |\langle N^* | M | N \rangle|^2 \left(1 - \frac{v_{thr}^2}{v^2}\right)^{1/2} = \sigma_I^{as} \left(1 - \frac{v_{thr}^2}{v^2}\right)^{1/2}, \quad (8)$$

with $\langle N^* | M | N \rangle$ being the matrix element for inelastic scattering. Details can be found in Ref. [25]. To incorporate effects of the finite size of the ^{129}Xe nucleus, the form factor $F^2(E_{nr})$ should be taken into account. In fact, there are several models on the form factor for ^{129}Xe including recent studies on the effect of uncertainties due to WIMP-nucleon currents [26–30]. In this paper, we chose same model [26] as DAMA group [12, 13] for comparison.

The resulting expected combinations of excitation and nuclear recoil are used to simulate events. In the simulation, scintillation light emission due to nuclear recoil (decay constant $\tau_{nr} = 25$ ns [31]) and the subsequent γ -ray emission due to de-excitation are simulated at their common vertex in the detector. Here we ignore the few percent difference of K shell and L shell electron ejection probability after de-excitation and gamma ray absorption. These vertices were distributed uniformly in the inner detector. The half life of the excited state can be ignored since it is much faster (~ 1 ns) than the decay constant of scintillation light. Figure 1 shows the resulting simulated energy deposits for WIMPs with various masses.

4. Data reduction and Optimization

The data used for this search was taken between December 24, 2010 and May 10, 2012, and amounts to a total live time of 165.9 days. Since we took extensive calibration data and various special runs to understand the background and the general detector response, we selected runs taken under what we designated “normal running conditions” with stable temperature and pressure (0.160-0.164 MPa absolute). Additional data quality checks reject runs with excessive PMT noise, unstable pedestal levels, or abnormal trigger rates.

As discussed in Ref. [16, 17], most of the observed events are background events due to radioactive contamination in the aluminum seals of our PMTs and radon progeny on the

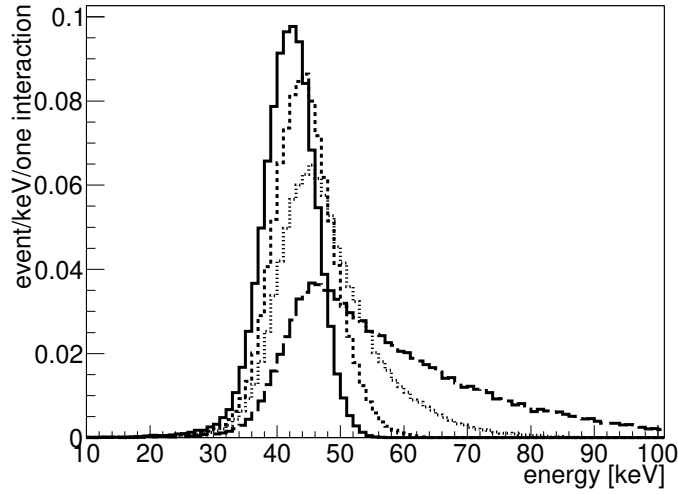


Fig. 1 Simulated energy spectra for the WIMP mass with 20 (solid line), 50 (dashed line), 100 (dotted line), and 1000 GeV (long dashed line). The energy is defined by dividing the number of p.e. observed by 13.9 (p.e./keV).

inner surface of the detector. To reduce these backgrounds, a dedicated event reduction procedure was developed for this analysis. In this section we give a detailed description of this reduction procedure and our evaluation of its acceptance.

Data reduction proceeds in four steps: (1) Pre-selection. This is similar to Ref. [16]. One difference is that events occurring less than 10 ms prior to an event as well as following the event are rejected since events caused by ^{214}Bi , a daughter of ^{222}Rn , must be removed. (2) Fiducial volume (radius) cut. As is described in Ref. [15], the observed pattern of p.e. is used to reconstruct an event vertex. The radial position R of an event is obtained from this reconstruction. (3) Timing cut. Even after the radius cut, some surface events remain in the sample. Timing information is used to further reduce these remaining surface background events. Here we use the timing difference δT_m between the first hit and an average of hit timings of first 50% PMT signals except for first 10 hits. A larger timing difference is indicative of a surface event. (4) Band cut. Grooves and gaps exist between PMTs. Scintillation light caused by events inside those grooves have a characteristic pattern. This pattern emerges because the propagation of scintillation light from within a groove is constrained by the rims of the groove, and its characteristic band shape can be identified. Events with such a pattern are eliminated by this cut. An axis is defined by the geometric center of the detector and the reconstructed event vertex. This axis intersects the approximately spherical inner detector surface in two opposing points. We select PMTs within bands extending $\pm 7.5\text{ cm}$ around great circles through these two points. In a first step we determine the great circle for which the p.e. count of the PMTs within in its band becomes maximal. We next check planes parallel to that in which the selected great circle lies in an effort to further maximize the integral p.e. count on PMTs within a 15 cm wide band around these parallel planes. Again we select the plane with the maximal p.e. count in its 15 cm wide band. This determines the

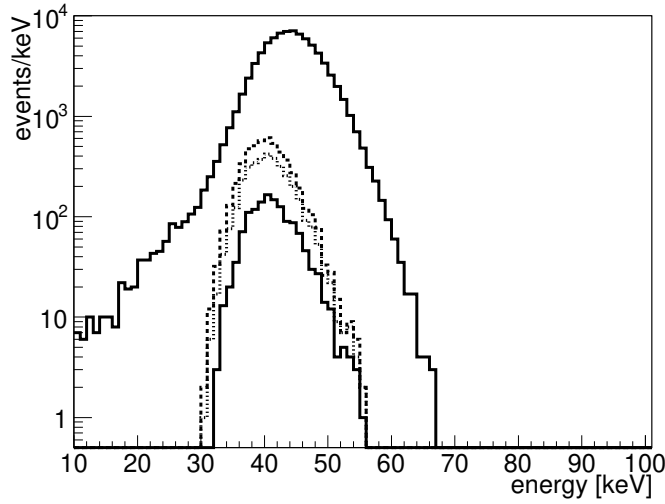


Fig. 2 Energy spectra of the simulated events after each step of the cuts for 50 GeV WIMP. From top to bottom, simulated energy spectrum after the preselection (solid line), cut (2) (dashed line), cut (3) (dotted line), and cut (4) (solid line). As we do not apply the proper radial correction for energy, a shift in our energy scale seems to occur after our fiducial volume cut (2). As we are only using events in a very limited fiducial volume and our energy scale is based on calibration at the center of the detector, the energy scale of the surviving events is correct within 4%.

maximal p.e. count in a 15 cm wide band, which defines our cut parameter as follows:

$$\text{Band cut parameter } F_B = \frac{\text{Maximum p.e. in a band of width 15 cm}}{\text{Total p.e. in the event}} \quad (9)$$

The cut values for the three cuts above were optimized for a WIMP mass of 50 GeV. Other than the radius cut our cut values were determined by optimizing the ratio of remaining signal events in a signal range from 30 to 80 keV from our simulation over the sum of background events in two side bands ranging from 10 to 30 and from 80 to 100 keV. For the radius cut this procedure results in an extremely low fiducial volume, leading us to relax the cut to 15 cm. For the remaining cuts the values resulting from our optimization were 12.91 ns for the timing cut and a ratio of 0.248 for the band cut. Events with parameter values smaller than these cut values were chosen for the final sample.

Fig. 2 and 3 show the impact of our cuts on the expected signal from our 50 GeV WIMP simulation and the observed data spectrum, respectively. The signal window is defined as 36-48 keV, so that it contains 90% of the 50 GeV WIMP signal. These cut values and signal window optimized for the 50 GeV WIMPs were also used to obtain the limits for the other WIMP masses. A signal efficiency is defined as the ratio between the number of simulation events remaining after all cuts in the 36-48 keV signal region and the number of simulated events generated within the fiducial volume (radius less than 15 cm). It ranges from 29% for 50 GeV WIMPs to 15% for 5 TeV WIMPs as shown in Table. 1.

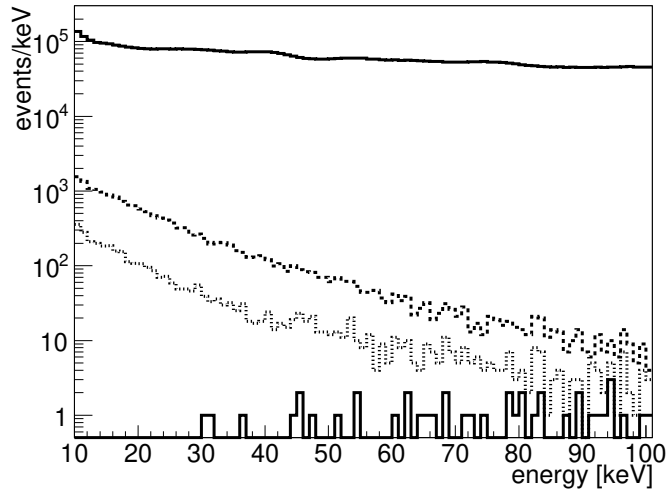


Fig. 3 Energy spectra of the observed events after each step of the cuts for our 165.9 days data. From top to bottom, the observed energy spectrum after the preselection (solid line), cut (2) (dashed line), cut (3) (dotted line), and cut (4) (solid line).

5. Results and Discussion

As clearly visible in Fig. 3, the cuts discussed in the previous section almost eliminate all background in and around the signal region. After all cuts 5 events are remaining in our 36 to 48 keV signal region. The main contribution to the remaining background in this energy region stems from the ^{222}Rn daughter ^{214}Pb . From our simulation we estimate this background alone to contribute 2.0 ± 0.6 events. As other background contributions are smaller but less certain, we do not subtract background when calculating our limits. We directly use the event count in the signal region to extract our limit on the inelastic scattering cross section of WIMPs on ^{129}Xe nuclei. Using Eq. 6 and taking into account the nuclear form factor and our signal efficiency we derive the 90% C.L. upper limit for this cross section which in Fig. 4 is compared to the result from [12, 13]. The gray band reflects our systematic uncertainties. The systematic uncertainty on our signal efficiency is estimated from data - MC comparisons for ^{241}Am calibration data (60 keV) at various positions within the fiducial volume. The relevant comparisons are shown in Figs. 5 and 6. From these comparisons we derive systematic differences in energy scale, energy resolution, radius reconstruction, timing cut and band cut parameter. There is uncertainty in the effective light yield \mathcal{L}_{eff} and the decay constants of nuclear recoils. The cumulative effect of these individual contributions is obtained by summation in quadrature.

As an example for our systematic error evaluation we explain it for the signal efficiency for 50 GeV WIMPs; see Table. 2 for other masses. The uncertainty in our energy scale evaluates to $\pm_{3.1}^{4.6}\%$ by comparing more than 10 sets of calibration data (^{57}Co), taken at different times throughout the data taking period, with our simulation. Changing the number of photons generated per unit energy deposited in the simulation by this amount, the signal efficiency changes by $\pm_{13}^{11}\%$. The uncertainty in the energy resolution, 12%, is evaluated by comparing the resolution of the 60 keV peak in the calibration data and simulated events. This led to

WIMP mass (GeV)	20	50	100	300	1000	3000	5000
signal efficiency (%)	$23 \pm_6^7$	$29 \pm_5^4$	$26 \pm_4^2$	$19 \pm_3^1$	$16 \pm_3^1$	$15 \pm_3^1$	$15 \pm_3^1$

Table 1 Signal efficiencies with their systematic errors for deriving the limit shown in Fig. 4.

a 5.6% reduction in the signal efficiency. The radial position of the reconstructed vertex for the calibration data differs by 5 mm from the true source position, which causes a 3.2% reduction in the efficiency. The band cut and the timing cut each have a slightly different impact on calibration data and simulated events. By taking the difference of their acceptance we evaluated the systematic impact on the signal efficiency as $\pm 4.2\%$ for the band cut and $\pm_{5.1}^{4.2}\%$ for the timing cut. The 1σ uncertainty in the effective light yield \mathcal{L}_{eff} changes the signal efficiency in a range from $+1.4\%$ to -0.2% . For the decay constants of scintillation light caused by nuclear recoils we took the uncertainty in the determination of the constants and the difference between our values and the NEST model [32], ± 1 ns, as our systematic uncertainty. The total systematic error on the signal efficiency for a 50 GeV WIMP was evaluated to $\pm_{16}^{13}\%$, summing up in quadrature the systematic errors as evaluated above. This evaluation was repeated for WIMP masses of 20, 100 and 300 GeV and 1, 3 and 5 TeV and assumed to be applicable for masses close to the evaluated ones.

Finally we evaluated the variation of our limit within our systematic uncertainties. Assuming a true number of events μ in the energy window before the event reduction, we can calculate the expected number of observed events by multiplying with the signal efficiency tabulated in Tab. 1. Based on the expected number of observed events, we can generate number of observed events following Poisson statistics. This procedure was repeated to accumulate a histogram of the observed number of events for a fixed μ by sampling the signal efficiency within its systematic error. The 90% C.L. upper limit for μ is the one that results in a 10% probability to have five events or less. Using Eq. 6 this is then translated to an inelastic WIMP nucleus cross section with the variation of our limit within our systematic uncertainties shown by the gray band in Fig. 4.

It should be noted that the constraint obtained by the DAMA group [12, 13] was derived from a statistical evaluation of an excess above a large background, $2 \times 10^{-2} \text{ keV}^{-1} \text{ d}^{-1} \text{ kg}^{-1}$. We achieved a lower background $\sim 3 \times 10^{-4} \text{ keV}^{-1} \text{ d}^{-1} \text{ kg}^{-1}$ using the cut discussed above. This low background allowed us to avoid having to subtract background to obtain a competitive limit.

6. Conclusion

A search for inelastic scattering of WIMPs on ^{129}Xe was performed using data from our single phase liquid xenon detector XMASS. The central volume within 15 cm of the XMASS detector containing 41 kg of LXe was used in this analysis. We observed no significant excess in 165.9 days' data and derived for e.g. a 50 GeV WIMP an upper limit for its inelastic cross section on ^{129}Xe nuclei of 3.2 pb at the 90% confidence level.

WIMP mass (GeV)	20	50	100	300	1000	3000	5000
Energy scale	\pm_{22}^{30}	\pm_{13}^{11}	$\pm_{5.1}^0$	$\pm_{7.1}^{0.4}$	$\pm_{9.5}^{1.1}$	$\pm_{11}^{2.2}$	$\pm_{11}^{2.7}$
Energy resolution	$\pm_{8.2}^0$	$\pm_{5.6}^0$	$\pm_{6.8}^0$	$\pm_{8.1}^0$	$\pm_{9.7}^0$	$\pm_{8.8}^0$	$\pm_{9.0}^0$
Radius cut	$\pm_{3.3}^0$	$\pm_{3.2}^0$	$\pm_{4.0}^0$	$\pm_{5.2}^0$	$\pm_{6.8}^0$	$\pm_{6.3}^0$	$\pm_{6.4}^0$
Timing cut	$\pm_{5.1}^{4.2}$	$\pm_{5.1}^{4.2}$	$\pm_{5.1}^{4.2}$	$\pm_{5.1}^{4.2}$	$\pm_{5.1}^{4.2}$	$\pm_{5.1}^{4.2}$	$\pm_{5.1}^{4.2}$
Band cut	$\pm_{4.2}$	$\pm_{4.2}$	$\pm_{4.2}$	$\pm_{4.2}$	$\pm_{4.2}$	$\pm_{4.2}$	$\pm_{4.2}$
\mathcal{L}_{eff}	$\pm_{0}^{6.4}$	$\pm_{0.2}^{1.4}$	$\pm_{1.4}^0$	$\pm_{0}^{3.9}$	$\pm_{1.3}^{1.0}$	$\pm_{1.7}^0$	$\pm_{4.0}^0$
τ_{nr}	$\pm_{0.8}^0$	$\pm_{2.2}^{1.3}$	$\pm_{8.8}^0$	$\pm_{4.6}^0$	$\pm_{4.7}^0$	$\pm_{5.7}^0$	$\pm_{5.7}^0$
total systematic error	\pm_{25}^{31}	\pm_{16}^{13}	$\pm_{15}^{5.9}$	$\pm_{14}^{7.1}$	$\pm_{17}^{6.0}$	$\pm_{18}^{6.3}$	$\pm_{18}^{6.5}$

Table 2 Systematic error on the signal efficiency for different WIMP masses. All the numbers tabulated are in % relative to the nominal efficiencies. They were evaluated by comparing ^{241}Am data and simulated events (see text).

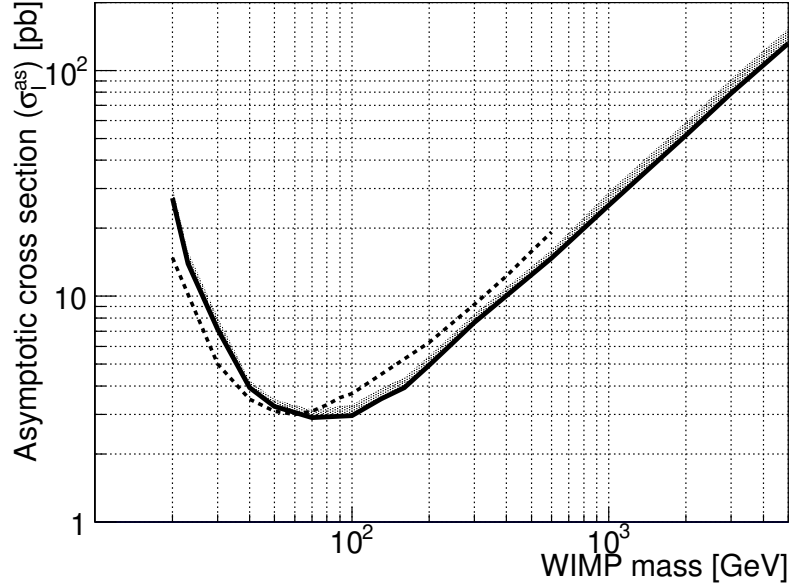


Fig. 4 The black solid line is our 90% C.L. upper limit on the asymptotic cross section σ_I^{as} for inelastic scattering on ^{129}Xe (black solid line). The gray band covers its variation with our systematic uncertainty. The dotted line is the limit obtained by the DAMA group [12, 13] derived from a statistical evaluation of an excess above its background.

Acknowledgements

We gratefully acknowledge the cooperation of Kamioka Mining and Smelting Company. This work was supported by the Japanese Ministry of Education, Culture, Sports, Science and Technology, Grant-in-Aid for Scientific Research, and partially by the National Research Foundation of Korea Grant funded by the Korean Government (NRF-2011-220-C00006). We thank Dr. Masahiro Ibe for useful discussion.

References

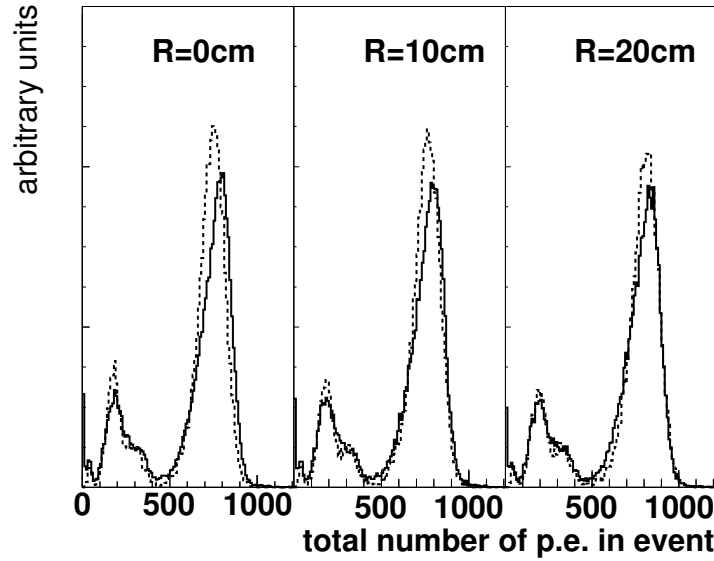


Fig. 5 Comparison between data (solid histograms) and simulation (dashed histograms) of the energy distribution of ^{241}Am at three radial positions R .

- [1] R. Bernabei *et al.*, Eur. Phys. J. C **56**, 333 (2008).
- [2] R. Bernabei *et al.*, Eur. Phys. J. C **67**, 39 (2010).
- [3] C. E. Aalseth *et al.*, Phys. Rev. Lett. **106**, 131301 (2011).
- [4] G. Angloher *et al.*, Eur. Phys. J. C **72**, 1971 (2012).
- [5] E. Aprile *et al.*, Phys. Rev. Lett. **109**, 181301 (2012).
- [6] J. Angle *et al.*, Phys. Rev. Lett. **107**, 051301 (2011).
- [7] Z. Ahmed *et al.*, Science **327**, 1619 (2010).
- [8] Z. Ahmed *et al.*, Phys. Rev. Lett. **106**, 131302 (2011).
- [9] E. Armengaud *et al.*, Phys. Rev. D **86**, 051701(R) (2012).
- [10] H. Ejiri, K. Fushimi, and H. Ohsumi, Phys. Lett. B **317**, 14 (1993).
- [11] K. Fushimi *et al.*, Nucl. Phys. B (Proc. Suppl.) **35**, 400 (1994).
- [12] P. Belli *et al.*, Phys. Lett. B **387**, 222 (1996).
- [13] R. Bernabei *et al.*, New J. Phys. **2**, 15 (2000).
- [14] Y. Suzuki, arXiv:hep-ph/0008296.
- [15] K. Abe *et al.*, (XMASS Collaboration), Nucl. Instr. Meth. A **716**, 78 (2013).
- [16] K. Abe *et al.*, (XMASS Collaboration), Phys. Lett. B **719**, 78 (2013).
- [17] K. Abe *et al.*, (XMASS Collaboration), Phys. Lett. B **724**, 46 (2013).
- [18] S. Fukuda *et al.*, (Super-Kamiokande Collaboration), Nucl. Instrum. Meth. A **501**, 418 (2003).
- [19] S. Agostinelli *et al.*, Nucl. Instr. Meth. A **506**, 250 (2003).
- [20] K. Amako *et al.*, IEEE Trans. Nucl. Sci. **53**, 270 (2006).
- [21] E. Aprile *et al.*, Phys. Rev. Lett. **107**, 131302 (2011).
- [22] J. Beringer *et al.*, (Particle Data Group), Phys. Rev. D **86**, 010001 (2012).
- [23] G. Jungman *et al.*, Phys. Rep. **267**, 195 (1996).
- [24] K. Freese *et al.*, Phys. Rev. D **37**, 3388 (1988).
- [25] J. Ellis *et al.*, Phys. Lett. B **212**, 375 (1988).
- [26] J. Engel, Phys. Lett. B **264**, 114 (1991).
- [27] P. Toivanen *et al.*, Phys. Lett. B **666**, 1 (2008).
- [28] P. Toivanen *et al.*, Phys. Rev. C **79**, 044302 (2009).
- [29] P. Klos *et al.*, Phys. Rev. D **88**, 083516 (2013).

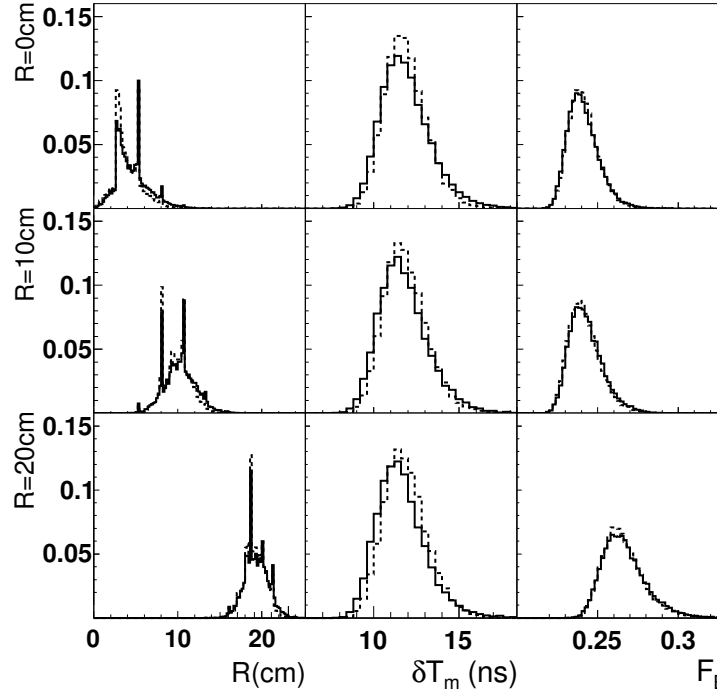


Fig. 6 Comparison between ^{241}Am data (solid histograms) and simulation (dashed histograms) for the three cut parameters at three radial positions in the detector, $R = 0$ cm, 10 cm, and 20 cm, from the top to the bottom, respectively. From left to right the distributions for all three parameters, the reconstructed radius, the timing difference, and the band cut parameter, are shown for each of the source positions.

- [30] L. Baudis *et al.*, arXiv:1309.0825 accepted for publication in Phys. Rev. D.
- [31] K. Ueshima, 2010, *Study of pulse shape discrimination and low background techniques for liquid xenon dark matter detectors*, PhD dissertation, University of Tokyo, Japan.
- [32] M. Szydagis *et al.*, JINST 6 (2011) P10002; NEST (Noble Element Simulation Technique), <http://nest.physics.ucdavis.edu/site/>.